Detection of bladder metabolic artifacts in (18)F-FDG PET imaging.

Geoffrey Roman-Jimenez, Renaud De Crevoisier, Julie Leseur, Anne Devillers, Juan David Ospina, Antoine Simon, Pierre Terve, Oscar Acosta

Detection of bladder metabolic artifacts in ^{18}F-FDG PET imaging

Geoffrey Roman-Jimenez[a,b,d,*], Renaud De Crevoisier[a,c], Julie Leseur[c], Anne Devillers[c], Juan David Ospina[a,b], Antoine Simon[a,b], Pierre Terve[d], Oscar Acosta[a,b]

[a] *INSERM, U1099, Rennes, F-35000*
[b] *Université de Rennes 1, LTSI, Rennes, F-35000*
[c] *Département de Radiothérapie, Centre Eugène Marquis, Rennes, F-35000*
[d] *Keosys Medical Imaging, Saint-herblain, F-44815*

Abstract

Positron emission tomography using ^{18}F-fluorodeoxyglucose (^{18}F-FDG-PET) is a widely-used imaging modality in oncology. It enables significant functional information to to be included in analyses of anatomical data provided by other image modalities. Although PET offers high sensitivity in detecting suspected malignant metabolism, ^{18}F-FDG uptake is not tumor-specific and can also be fixed in surrounding healthy tissue, which may consequently be mistaken as cancerous. PET analyses may be particularly hampered in pelvic-located cancers by the bladder's physiological uptake potentially obliterating the tumor uptake. In this paper, we propose a novel method for detecting ^{18}F-FDG bladder artifacts based on a multi-feature double-step classification approach. Using two manually-defined seeds (tumor and bladder), the method consists of a semi-automated double-step clustering strategy that simultaneously takes into consideration standard uptake values (SUV) on PET, Hounsfield values on computed tomography (CT), and the distance to the seeds. This method was performed on 52 PET/CT images from patients treated for locally-advanced cervical cancer. Manual delineations of the bladder on CT images were used in order to evaluate bladder uptake detection capability. Tumor preservation was evaluated using a manual segmentation of the tumor, with a threshold of 42% of the maximal uptake within the tumor. Robustness was assessed by randomly selecting different initial seeds. The classification averages were 0.94 ± 0.09 for sensitivity, 0.98 ± 0.01 specificity, and 0.98 ± 0.01 accuracy. These results suggest this method is able to detect most ^{18}F-FDG bladder metabolism artifacts while preserving tumor uptake, and could thus be used as a pre-processing step for further non-parasitized PET analyses.

Keywords: Image Processing, PET/CT, bladder artifact, cervical cancer, radiotherapy, nuclear medicine

1. Introduction

In the last few decades, positron emission tomography/computed tomography (PET/CT) has been increasingly employed in cancer management,enabling the simultaneous assessment of tumor metabolic and morphological characteristics [1][2]. Of the different techniques, ^{18}F-fluorodeoxyglucose (^{18}F-FDG) PET imaging is now widely used to improve target delineation accuracy [3], diagnostic accuracy [4][5] as well as early outcome prediction in forms of cancer [6][7][8][9] that require accurate delimitation and precise quantification of tumor metabolism. PET imaging techniques' weak points are low spatial resolution, partial volume effect, low contrast, and high noise features. Also, despite PET being highly sensitive for detecting malignant metabolism, FDG uptake is not specific to tumor activity. ^{18}F-FDG fixation can be observed both in healthy tissue and benign dis-

*Corresponding author
Email address: geoffrey.roman-jimenez@keosys.com (Geoffrey Roman-Jimenez)

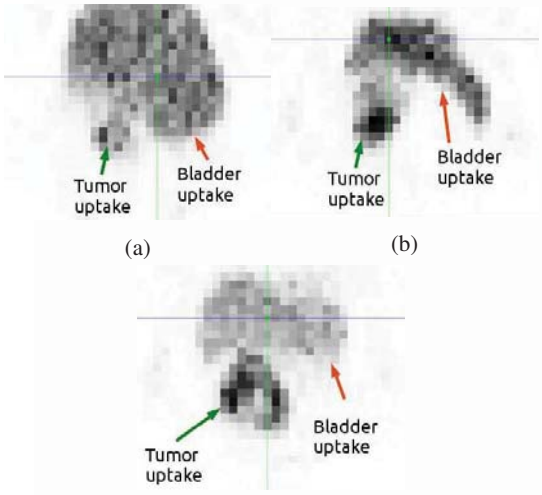

Figure 1: Three examples of PET acquisition of locally-advanced cervical cancer, demonstrating a continuum uptake between tumor and bladder hyperfixation

eases like inflammation, which can thereby be mistaken for cancer [10].

Today, numerous methodologies for ^{18}F-FDG PET segmentation have been proposed in the scientific literature using region-growing thresholds, edge detection, clustering, stochastic models, and deformable models, among other approaches [11][12][13][14]. However, despite the accuracy achievable with these recent methodologies, most are based solely on the PET data, leading to the possibility of including non-tumor ^{18}F-FDG uptake in the resulting segmentations.

When particularly considering cancers located in the pelvic region, PET analyses may be especially hampered by physiological uptake in the bladder, which could be a confounder for tumor uptake [15]. Due to the bladder's natural flow mechanics of filling and emptying, ^{18}F-FDG uptake can vary, thereby generating a similar PET signal for the bladder to that of a tumor. Fig. 1 presents three cases of locally-advanced cervical tumors with continuum uptake within the bladder.

To avoid ^{18}F-FDG bladder hyperfixation, patients are invited to empty their bladder before commencing ^{18}FDG PET/CT scanning [16]. In rare cases, urinary catheters can be used to ensure the bladder is empty for the PET acquisition. Nevertheless, urinary catheter positioning is known to be difficult and carries a non-negligible risk of increased irradiation damage [17].

Bladder uptake may also be suppressed by using expert manual bladder CT delineation. However, manual delineations are known to be laborious, subjective and inter-observer dependant [11].

Current clinical practice involves manually positioning a 3D-box encompassing the lesion to avoid adjacent structures [18][19][20][21]. Nevertheless, the 3D-box needs to be large enough to contain the entire tumor metabolism but also as small as possible to reduce high signals damaging neighboring tissues. Evidently, these procedures involve inter- and intra-user variability and can include voxel artifacts depending on the proximity and shape of the bladder.

To the best of our knowledge, no other automatic or semi-automatic method for detecting metabolism artifacts with the aim of improving and simplifying pelvic PET analysis have previously been proposed. In this paper we present a semi-automatic method for detecting ^{18}F-FDG bladder artifacts using a double-step clustering approach that simultaneously exploits multimodal PET-CT data and *a priori* spatial information. The k-means algorithm was used to ensure an unsupervised clustering and low computational cost. As bladder uptake is not systematically found in these procedures, our detection method could be considered a pre-processing step for PET imaging in order to enable further non-parasitized tumor quantification. From this point of view, the issue we wish to address herein is how to distinguish the bladder signal while preserving the information arising from the tumor uptake. This methodology was applied to real clinical data from a standardized clinical protocol where bladder uptake was observed in several cases.

The paper is structured as follows: Section 2 introduces the overall framework of the study; Section 2.2 exposes each step of the proposed methodology, followed by validation based on the clinical data; Section 3 presents the results; Section 4 presents our discussion and conclusions.

2. Material and Methods

The overall framework of our proposed methodology for semi-automatically detecting the bladder metabolic artifacts is presented in Fig. 2. This method is divided into

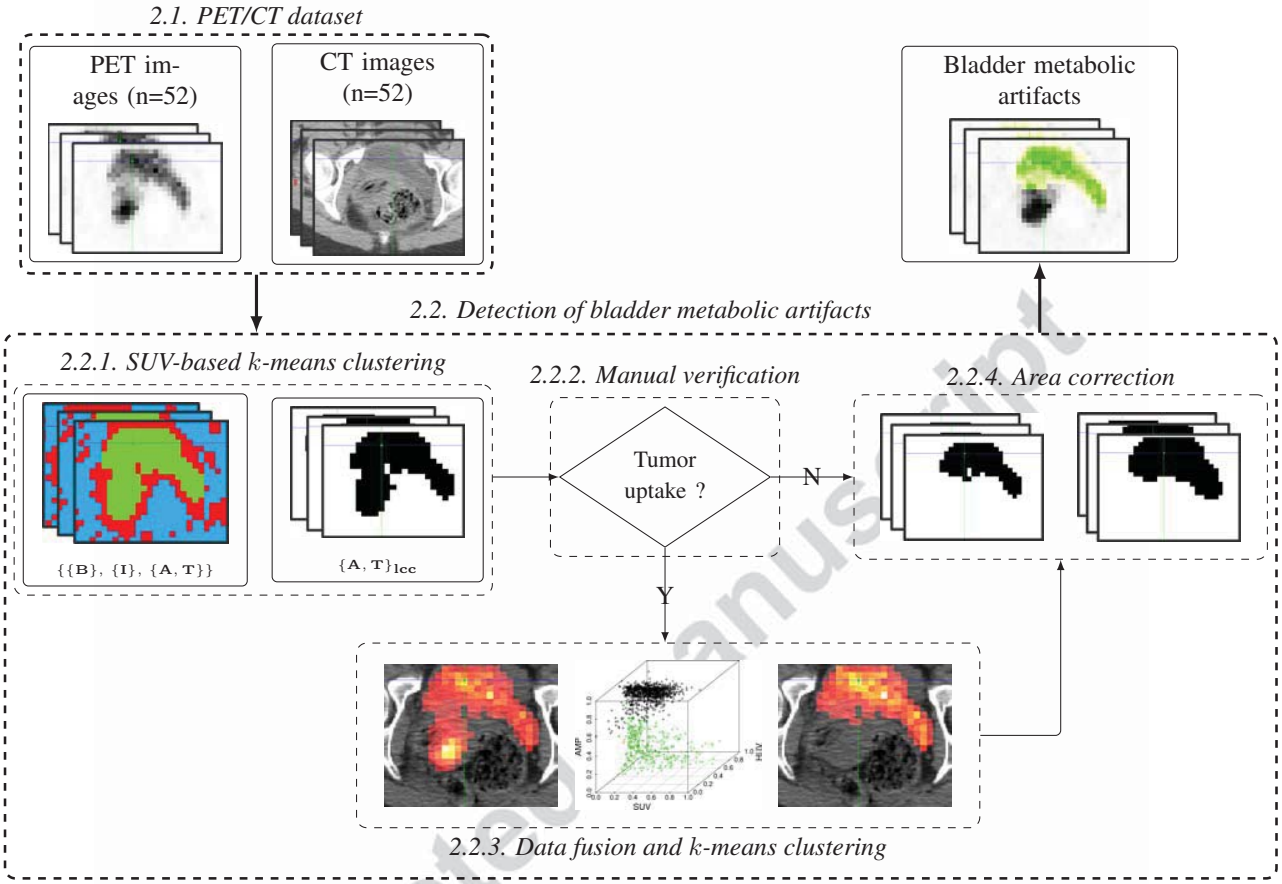

Figure 2: Overall framework of the proposed methodology for semi-automatically detecting the bladder metabolic artifacts. First, k-means clustering was performed using only PET intensity to roughly select the voxels with the highest values, likely belonging to the tumor or bladder (2.2.1). Following manual verification (2.2.2), an optional second step of clustering using PET/CT data and *a priori* spatial information was performed was performed (2.2.3). Finally, morphological correction was applied to ensure the topological compactness of the detected region (2.2.4)

two major clustering steps. First, k-means clustering was performed using only PET intensity to roughly select the voxels with the highest values, likely to be those belonging to the tumor or bladder (2.2.1). The largest connected component in the resulting cluster was then considered for the next step. Manual inspection was conducted to verify if tumor metabolism could be visually detected in the resulting area (2.2.2). If so, a second step of clustering was performed using PET/CT data and *a priori* spatial information (2.2.3). Morphological correction was then applied to ensure the topological compactness of the detected region (2.2.4). Validation (2.3) was conducted on a dataset of 52 PET/CT images by: i) comparing the detected bladder voxel artifacts using expert manual bladder CT delineation; ii) comparing tumor metabolism preservation with respect to a segmentation on PET images using the commonly-used threshold of 42% of the maximum uptake within the tumor ($T42$).

The clustering algorithms and segmentations were carried out using the C++ library Insight Segmentation and Registration Toolkit (ITK).

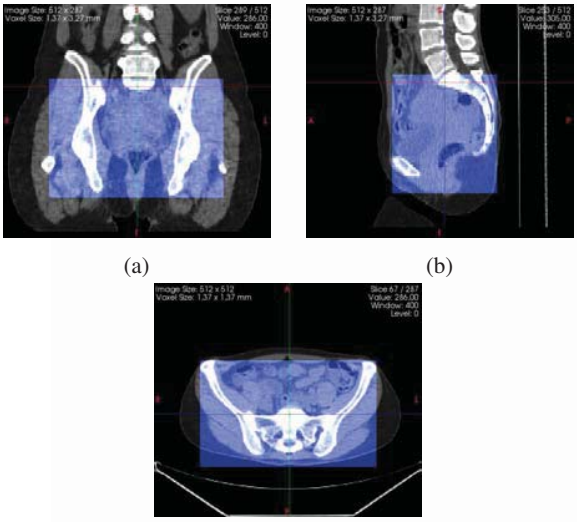

(a) (b)

(c)

Figure 3: Example of pelvic region cropped according to coxal bone structures on CT images

2.1. PET/CT dataset

We initially included 52 patients (median age: 52.44 years [32.15 - 84.62]) with locally-advanced cervical cancer treated at the Centre Eugene Marquis (CEM), Rennes, France. All were treated using external beam radiation therapy with concurrent cisplatin chemotherapy followed by brachytherapy.

Each patient underwent an ^{18}F-FDG PET/CT scan prior to treatment. Patients were invited to void before imaging. No intravenous contrast was used during the CT acquisitions.

Each voxel from the PET scan was converted into a standardized uptake value (SUV) for comparisons across patients. The SUV is a standardized decay-corrected value of ^{18}F-FDG activity per unit volume of body weight (MBq/kg) [22]. The full-body PET/CT images were cropped to the pelvic region based on the coxal bone structures visualized on CT imaging. The box boundaries were delimited according to well-defined landmarks that could be easily reproducible. Fig. 3 depicts an example of a cropped pelvic region.

2.2. Detection of bladder metabolic artifacts

We defined bladder metabolic artifact (BMA) as areas where the ^{18}F-FDG bladder activity was highest and comparable to that originating from the tumor. We defined the calculation of BMA detection as a classification formula where each voxel of the PET image was assigned to one of the three clusters of Set $\mathbf{S}$:

$$\mathbf{S} = \{\{B\}, \{I\}, \{A, T\}\}, \tag{1}$$

where $\{B\}$ and $\{I\}$ refer to the voxels producing very low and intermediate uptake values, respectively. Cluster $\{A, T\}$ refers to very high uptake voxels, which may belong to either tumor $\{T\}$ or non-tumor $\{A\}$ classes, respectively.

The BMA detection sought to accurately identify the voxels belonging to $\{A\}$. It should be noted that $\{T\}$ does not correspond to tumor segmentation but only to voxels with high uptake, which thus likely belong to a tumor and should be preserved for further non-parasitized quantitative analyses.

Due to the bladder shapes observed, we assumed that the BMA revealed in PET imaging was a topologically compact object. Two voxels roughly representing the bladder and tumor barycenter were selected, denoted s_b and s_t, respectively.

2.2.1. SUV-based k-means clustering

In our calculations, $\mathbf{X} = \{x_1, x_2, ..., x_n\}$ the set of n voxels on the PET image.

In general terms, the k-means algorithm aims to partition the n voxels of $\mathbf{X}$ into k clusters by minimizing the within-cluster sum of squares difference:

$$\underset{C}{arg\,min} \sum_{j=1}^{k} \sum_{x_i \in c_j} \|x_i - \mu_j\|^2, \tag{2}$$

where $\mathbf{C} = \{c_1, c_2, ..., c_k\}$ is the set of clusters and μ_j denotes the mean of voxels in c_j. With cluster set $\mathbf{S}$, the objective function becomes:

$$\begin{aligned} \underset{S}{arg\,min} & \sum_{x_i \in \{B\}} \|x_i - \mu_B\|^2 + \sum_{x_i \in \{I\}} \|x_i - \mu_I\|^2 \\ & + \sum_{x_i \in \{A,T\}} \|x_i - \mu_{A,T}\|^2, \end{aligned} \tag{3}$$

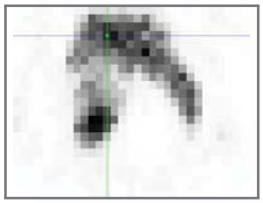

(a)

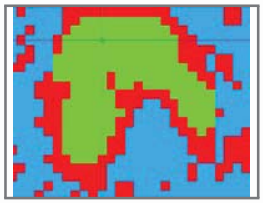

(b)

Figure 4: SUV-based k-means clustering example. (a) Original PET exam. (b) k-means clustering result: (green) corresponds to Cluster $\{A, T\}$, (red) to Cluster $\{I\}$, and (blue) to Cluster $\{B\}$

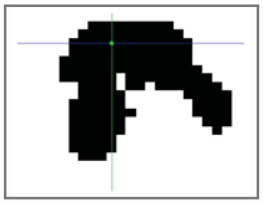

(a)

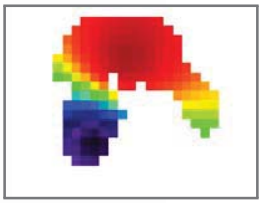

(b)

Figure 5: (a) Cluster $\{A, T\}_{lcc}$ and (b) the corresponding AMP for each voxel in $\{A, T\}_{lcc}$: (red) corresponds to AMP=1 and (black) to AMP=0.

Fig. 4 presents an example of an SUV-based k-means clustering with cluster set $\mathbf{S}$.

As the SUV-based k-means clustering took no spatial information into consideration, we selected the largest connected component (lcc) of Cluster $\{A, T\}$ connected to seed s_b to avoid distant regions and ensure that the resulting area was only related to the BMA. The resulting cluster was labeled $\{A, T\}_{lcc}$.

Fig. 5a presents an example of Cluster area $\{A, T\}_{lcc}$.

2.2.2. *Manual verification*

The potential presence of tumor metabolism in Cluster $\{A, T\}_{lcc}$ was determined visually. If no tumor metabolism was present in $\{A, T\}_{lcc}$, the cluster was denoted as just $\{A\}$. If tumor metabolism was visually detected in $\{A, T\}_{lcc}$, a second step of clustering using CT information and *a priori* information was performed with the intention of splitting $\{A\}$ from $\{T\}$.

2.2.3. *Data fusion and k-means clustering*

In the second clustering step, a k-means algorithm was applied for further classification of Set $\{A, T\}_{lcc}$, based on a simultaneous exploitation of CT Hounsfield units, PET SUVs, and normalized distance maps. The distance map was built as an artifact membership probability (AMP) as follows:

$$AMP(x_i) = 1 - \frac{d^2(x_i, s_b)}{d^2(x_i, s_t) + d^2(x_i, s_b)}, \qquad (4)$$

where $d^2(x_i, s_t)$ and $d^2(x_i, s_b)$ are the squared Euclidean distances of voxel x_i from seed s_t and seed s_b, respectively.

The hypothesis behind the AMP relies on the concept that the further the voxel is from the tumor seed, the lower the probability of it belonging to the artifacts. Similarly, we assumed that the closer the voxel was to the bladder seed, the higher the probability of it belonging to the bladder artifacts.

An example of AMP computed for each voxel in $\{A, T\}_{lcc}$ is illustrated in Fig. 5b.

From each x_i clustered in $\{A, T\}_{lcc}$, three features were considered: the SUV from the PET, labeled U_i; the Hounsfield unity value (HUV) from the CT, labeled H_i; the AMP, labeled P_i. The SUVs and HUVs were normalized between 0 and 1. We denoted $\mathbf{V}_{\{A,T\}_{lcc}} = \{\mathbf{v}_i\}$ the group of vector $\mathbf{v}_i = (U_i\ H_i\ P_i)^T$.

Fig. 6a represents an example of $\mathbf{V}_{\{A,T\}_{lcc}}$ projected in the tri-parametric space $[SUV\ HUV\ AMP]$.

Each $\mathbf{v}_i$ was assigned a label stating if it belonged to cluster $\{T\}$ or $\{A\}$, following the objective function below:

$$\underset{\{A,T\}_{lcc}}{arg\,min} \sum_{\mathbf{v}_i \in \{T\}} \|\mathbf{v}_i - \boldsymbol{\mu}_T\|^2 + \sum_{\mathbf{v}_i \in \{A\}} \|\mathbf{v}_i - \boldsymbol{\mu}_A\|^2 , \qquad (5)$$

Fig. 6b represents an example of the k-means clustering in the tri-parametric space $[SUV, HUV, AMP]$.

In accordance with the compactness hypothesis on the BMA shape, the largest connected component of the cluster connected with seed s_b was selected to be $\{A\}$.

2.2.4. *Area correction*

Topological transformations, namely closing and opening were applied to ensure the compactness of the resulting area formed by $\{A\}$. The resulting corrected area was

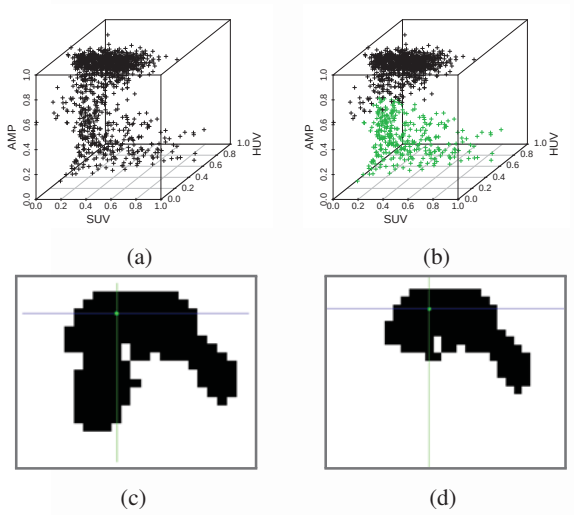

Figure 6: *Data fusion and k-means clustering* example. (a) voxels belonging to $\{A, T\}_{lcc}$ placed in the tri-parametric clustering space $[SUV \ \ HUV \ \ TMP]$: SUV value (SUV), Hounsfield unity value (HUV), and the artifact membership probability (AMP). (b) k-means clustering result: cluster $\{A\}$ in black and cluster $\{T\}$ in green. (c) Cluster $\{A, T\}_{lcc}$ and (d) the resulting cluster $\{A\}$.

labeled BMA. Fig. 7 presents an example of an area correction for obtaining the BMA.

2.3. Validation

2.3.1. Measures of performance of BMA detection

We measured the performance of the BMA detection carried out by the proposed algorithm in two phases. First, we considered solely an expert manual bladder CT delineation as ground-truth (true-positives) and computed the sensitivity, specificity and accuracy of the BMA detection. Secondly, we considered a tumor segmentation mask as the background (true-negatives) and computed the related sensitivity, specificity and accuracy in order to assess the algorithm's tumor preservation capability. The bladder was manually segmented by an expert on each CT image using the Phillips Pinnacle[3] Version 8.0m treatment planning software. The CT images were then linearly down-sampled to the PET resolution so that each PET voxel corresponded to only one voxel of the CT, and likewise for the bladder delineations. Tumor metabolic activities were segmented on PET images

Figure 7: Area correction example. (a) Cluster $\{A\}$. (b) Bladder metabolic artifact (BMA) following area correction.

by region-growing using a threshold of 42% of the maximum uptake within the tumor ($T42$). Residual bladder uptake in the $T42$ segmentation mask was suppressed by the corresponding manual bladder CT delineation.

The voxels outside the bladder mask were considered true negatives (TN), whereas the voxels within the bladder mask were the true positives (TP). The number of voxels originally located in the bladder and not detected as artifacts were labeled false negatives (FN). Lastly, the number of voxels originally localted outside the bladder mask and detected as artifacts were labeled false positives (FP).

In parallel, the detection was evaluated a second time using the T42 segmentation mask. The number of voxels detected as artifacts yet originally located inside the T42 mask were this time considered false positives (FP_{T42}), whereas the number of voxels in the T42 mask that were not detected as artifacts were labeled true negatives (TN_{T42}).

Fig. 8 illustrates the PET and CT delineations used to evaluate the detection of bladder metabolic artifacts performed by the proposed methodology.

For the sake of clarity, we describe below how we computed the measures of performance of the detection method for each PET image, namely sensitivity (SEN), specificities (SPE and SPE_{T42}) and accuracies (ACC and ACC_{T42}) :

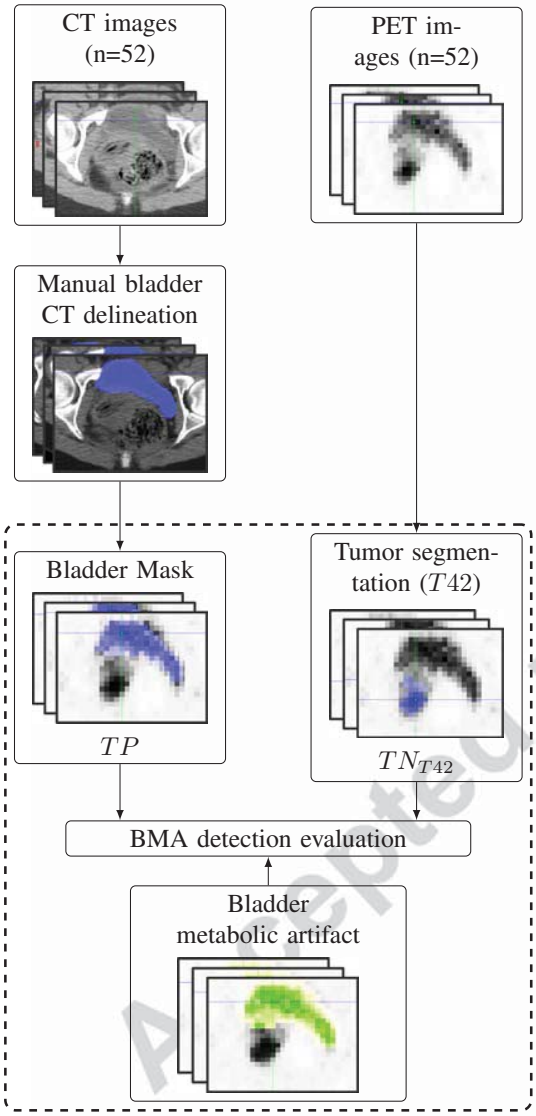

Figure 8: PET and CT delineations used for evaluating the BMA detection method. Bladder Mask: Expert manual bladder CT delineations linearly down-sampled to the PET resolution. Tumor Segmentation ($T42$): Metabolic activities segmented on PET images by region-growing using a threshold of 42% of the maximum uptake within the tumor

$$
\begin{aligned}
SEN &= \frac{TP}{TP+FN}, \\
SPE &= \frac{TN}{TN+FP}, \\
ACC &= \frac{TP+TN}{TP+TN+FP+FN}, \\
SPE_{T42} &= \frac{TN_{T42}}{TN_{T42}+FP_{T42}}, \\
ACC_{T42} &= \frac{TP+TN_{T42}}{TP+TN_{T42}+FP_{T42}+FN}.
\end{aligned}
\tag{6}
$$

2.3.2. Reproducibility evaluation

Reproducibility was assessed by randomly selecting 30 different seed pairs (s_b and s_t) within a 2×2×2-cm region around the initial manually-selected seeds. Thus, 30 different BMA detections were performed for each image.

3. Results

In this study, 47 out of 52 PET images presented tumor uptake in region $\{A,T\}_{lcc}$ and were considered in the second clustering step. Fig. 9 presents four examples of BMA detection using the proposed method.

The values attesting to the proposed detection method's performance (SEN, SPE, SPE_{T42} ACC and ACC_{T42}) for all PET images of our dataset have been presented using a boxplot representation in Fig. 10. For all 52 BMA detections evaluated, the averaged results were 0.94 ± 0.09 SEN, 0.98 ± 0.01 SPE and 0.98 ± 0.01 ACC. For the $T42$ segmentation, the averaged results were 0.97 ± 0.05 SPE_{T42} and 0.94 ± 0.08 ACC_{T42}.

In the 30 seed pairs randomly selected for each image, a total of 1,560 BMA detections (52×30) were obtained to enable assessment of the method's reproducibility.

For these BMA detections, the average SEN, SPE and ACC were 0.91 ± 0.13, 0.98 ± 0.02 and 0.98 ± 0.02, respectively. For the $T42$ mask, the average SEN values were the same, and the SPE_{T42} and ACC_{T42} averages were 0.96 ± 0.07 and 0.92 ± 0.12, respectively.

The overall robustness of the results for the whole cohort is depicted in Fig. 11. This demonstrates that for most of the seeds locations, the same segmentation was obtained. However, if the seed was located outside the

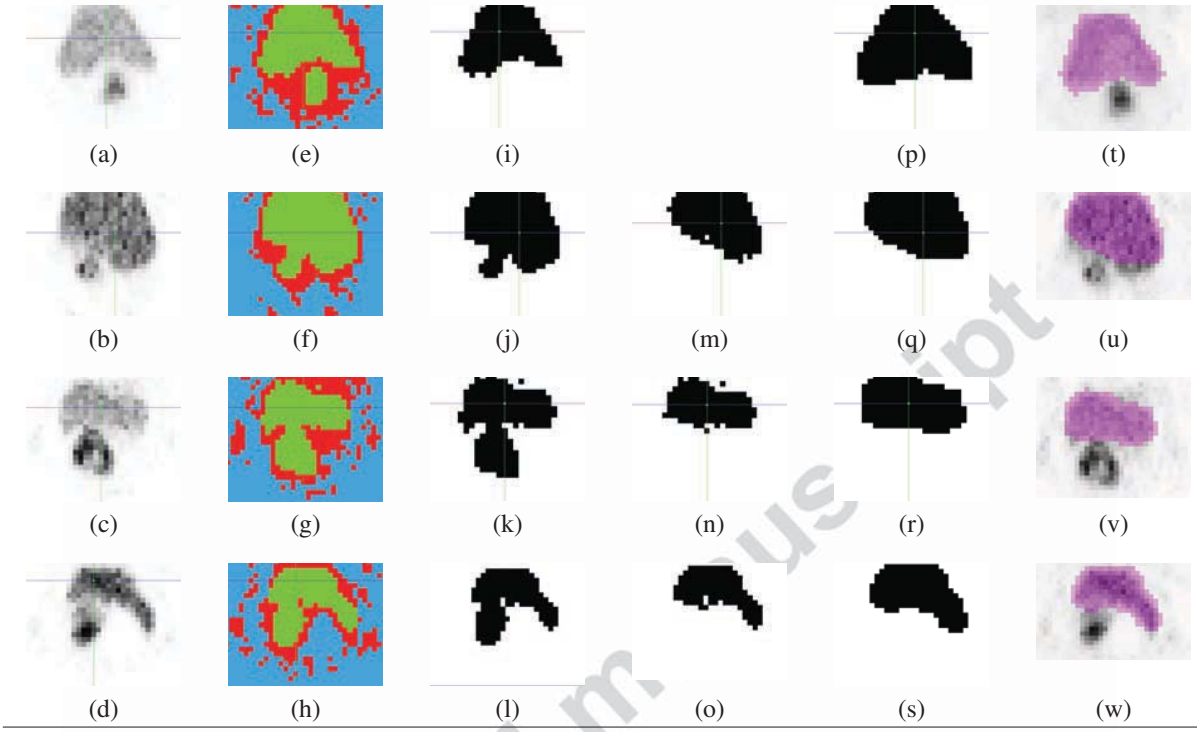

Figure 9: Example of BMA detection results for four patients. (a)-(d) Original PET exams. (e)-(h) 2.2.1 SUV-based k-means clustering results. (i)-(l) Clusters $\{A, T\}_{lcc}$. (m)-(o) cluster $\{A\}$ following 2.2.3 data fusion and k-means clustering. (p)-(s) BMA regions following 2.2.4 area correction. (t)-(w) PET image with BMA highlighted

bladder, the regions could naturally be erroneously detected. In some cases, SEN=0 due to the random placement of seed s_b outside the bladder.

4. Discussion & Conclusion

In PET images, ^{18}F-FDG fixation can be observed in healthy tissue and benign disease, which are consequently mistaken for cancer [10]. PET analysis can be particularly hampered in cancers involving the pelvic region by the physiological uptake of the bladder, which can obliterate the tumor uptake of lesions located in this area [15].

In this paper we propose a semi-automatic method to detect ^{18}F-FDG bladder artifacts in PET imaging of pelvic cancer using a k-means clustering approach by combining PET and CT information.

Artifact detection was considered to be a means of preprocessing PET voxel classification, and particular attention was paid to the preservation of tumor metabolism to enable further non-parasitized PET analyses.

The problem of detection was tackled by a two-step clustering relying on two assumptions. 1) That only the voxels with high intensity would hamper the analyses of tumor metabolism in PET imaging. To select these voxels, we applied an SUV-based clustering algorithm with three classes (low, intermediate, and high intensities). 2) That the bladder artifacts would be the sole artifacts detected among the previously-selected voxels. Therefore, the high-intensity voxels could belong to either artifacts or tumors. A second clustering step using CT and *a priori* information was then performed to separate voxels belonging to the artifacts from those belonging to tumor activity. As the number of classes was fixed, we used the k-means

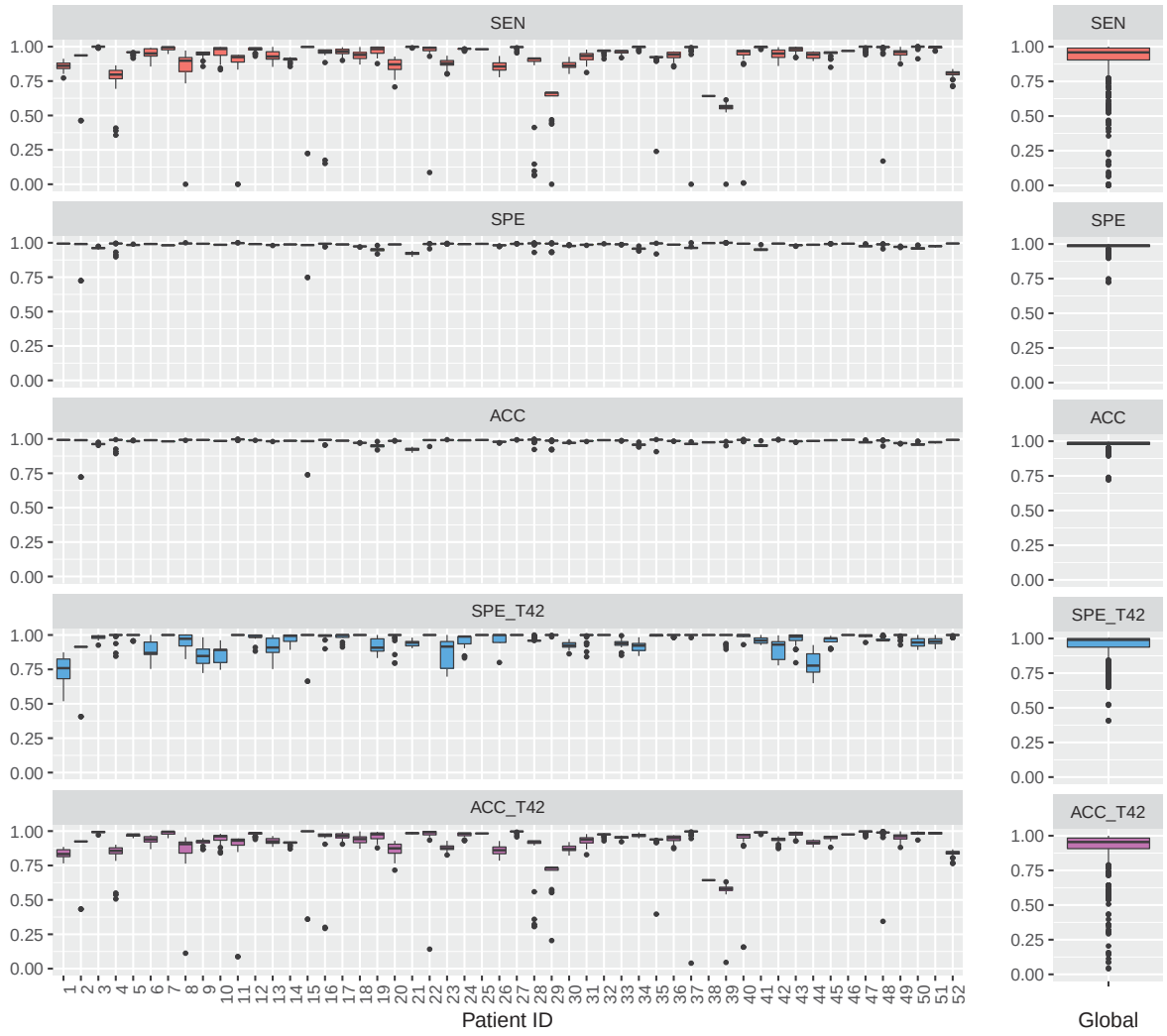

Figure 11: Overall results for the 52 patients for different seed locations. SEN, SPE, and ACC values correspond to the evaluation of the BMA detection method only considering bladder mask. SPE_{T42} and ACC_{T42} correspond to the evaluation of BMA detection performance using both bladder mask and $T42$ mask

algorithm to ensure unsupervised clustering and low computational cost. Nonetheless, for one given patient, we visually decided if the second classification step was necessary. Numerous other clustering algorithms have also been published in the literature [23]. For instance, the affinity propagation algorithm [24] or the density-based spatial clustering [25] could be used to automatically determine the number of clusters needed and, therefore, detect bladder artifacts in a one-step clustering process. Further investigation will be required to evaluate the use of such algorithms for the current challenge of reducing user dependency by automating the decision procedure.

Our proposed bladder artifact detection algorithm was tested on 52 PET/CT images of patients with locally-

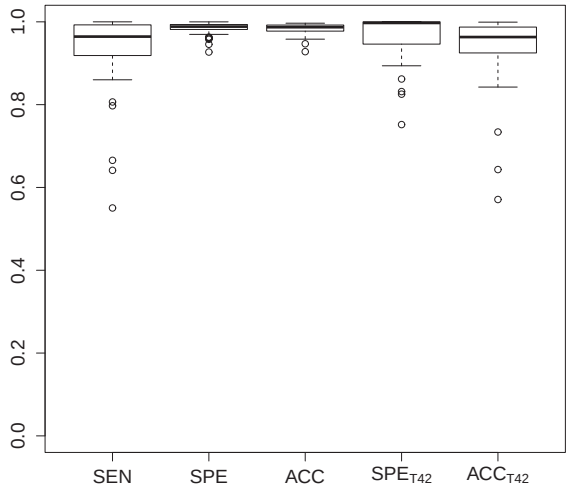

Figure 10: Values of the proposed algorithm's performance for the 52 PET images. SEN, SPE, and ACC corresponding to the evaluation of the BMA detection method, only considering bladder mask. SPE$_{T42}$ and ACC$_{T42}$ correspond to the evaluation of the BMA detection method considering both bladder mask and $T42$ mask.

advanced cervical cancer. We believe that the cancer's localization was relevant to our detection problem, as the bladder often presents an uptake continuum with the cervical tumor. However, in order to be applied to different pelvic cancer localizations, the algorithm would need to be adapted accordingly. To achieve this, further investigations should be carried out to evaluate the proposed method in other cancer localizations.

On our dataset of 52 PET images, only five were considered well-clustered following the first k-means clustering. This proves the interest of exploiting multimodal PET-CT data combined with *a priori* spatial information to distinguish bladder artifacts from tumor uptake.

We evaluated this proposed method firstly by comparing the detected bladder voxel artifacts with expert manual bladder CT delineation. Our results demonstrated the ability of the proposed method to classify voxels belonging to the bladder, with good average sensitivity, specificity, and accuracy (0.94±0.09, 0.98±0.01, and 0.98±0.01, respectively). We observed a lower sensitivity corresponding to a general underestimation of the bladder artifacts, which enabled the preservation of tumor activity. It should be noted that the ^{18}F-FDG uptake of the bladder did not systematically correspond to the bladder's anatomical shape. The bladder actually fills during PET image acquisition, as it takes several minutes, while CT data is acquired in a matter of seconds. Manual CT delineations used for evaluation are thus not strictly representative of the bladder's real metabolism.

The method was further evaluated using a threshold method often used in clinical practice ($T42$) as a region to spare. Specificity and accuracy were recomputed according to the $T42$ mask. It should be noted that $T42$ mask was not considered here as a ground truth of tumor metabolism, but rather as a reference enabling evaluation of the method's tumor-preservation capability. With its average specificity (SPET42) of 0.97±0.05 and accuracy (ACCT42) of 0.94±0.08, it demonstrated good conservation of tumor metabolism.

In order to initialize the second step of clustering to separate bladder voxels from tumor voxels, an artifact membership probability (AMP), derived from the squared Euclidean distance of the *a priori* tumor and bladder locations, was computed. We assumed, however, that the seeds were positioned near the barycenter of the bladder and tumor metabolism, positions that can lead to result variability. The robustness of the proposed algorithm was assessed by randomly selecting 30 different initial seeds for each of the 52 PET images. The overall averages indicate that the method is globally precise and robust for the seed initialization, achieving 0.91±0.13 SEN, 0.98±0.02 SPE, 0.98±0.02 ACC, 0.96±0.07 SPE$_{T42}$, and 0.92±0.12 ACC$_{T42}$. To reduce the variability, an alternative method that could be employed in future studies would be to include the possibility for users to select more seed points, thus incorporating more *a priori* information.

In conclusion, this proposed semi-automated method for detecting bladder metabolic artifacts on PET images of the pelvic region offers good preservation of tumor metabolism. This method can be used as a preprocessing step for further non-parasitized analyses.

Conflict of interest statement

None Declared.

[1] T. Z. Belhocine, P. Grisby, FDG PET and PET-CT in uterine cancers, Cancer Therapy 3 (2005) 201–18.

[2] B. J. Krause, S. Schwarzenböck, M. Souvatzoglou, FDG PET and PET/CT, Recent results in cancer research. Fortschritte der Krebsforschung. Progrès dans les recherches sur le cancer 187 (2013) 351–369, PMID: 23179888. doi:10.1007/978-3-642-10853-2˙12.

[3] M. MacManus, U. Nestle, K. E. Rosenzweig, I. Carrio, C. Messa, O. Belohlavek, M. Danna, T. Inoue, E. Deniaud-Alexandre, S. Schipani, et al., Use of pet and pet/ct for radiation therapy planning: Iaea expert report 2006–2007, Radiotherapy and oncology 91 (1) (2009) 85–94.

[4] R. Bar-Shalom, N. Yefremov, L. Guralnik, D. Gaitini, A. Frenkel, A. Kuten, H. Altman, Z. Keidar, O. Israel, Clinical performance of pet/ct in evaluation of cancer: additional value for diagnostic imaging and patient management, Journal of nuclear medicine 44 (8) (2003) 1200–1209.

[5] V. Kumar Dhingra, P. Kand, S. Basu, Impact of fdg-pet and-pet/ct imaging in the clinical decision-making of ovarian carcinoma: an evidence-based approach, Women's Health 8 (2) (2012) 191–203.

[6] J. Leseur, A. Devillers, J. O. Arango, D. Williaume, I. Lecouillard, J. Léveque, G. Louvel, K. Gnep, E. Garin, R. D. Crevoisier, Metabolic Monitoring by 18F-FDG PET during Radio-chemotherapy for Locally Advanced Cervical Cancer: Predicting Outcome, International Journal of Radiation Oncology*Biology*Physics 81 (2, Supplement) (2011) S47 – S48, proceedings of the American Society for Radiation Oncology 53rd Annual Meeting ASTRO's 53rd Annual Metting. doi:10.1016/j.ijrobp.2011.06.096.

[7] J. George, P. Claes, K. Vunckx, S. Tejpar, C. M. Deroose, J. Nuyts, D. Loeckx, P. Suetens, A textural feature based tumor therapy response prediction model for longitudinal evaluation with PET imaging, in: Biomedical Imaging (ISBI), 2012 9th IEEE International Symposium on, 2012, pp. 1048–1051. doi:10.1109/ISBI.2012.6235738.

[8] S.-H. Shim, D.-Y. Kim, D.-Y. Lee, S.-W. Lee, J.-Y. Park, J. Lee, J.-H. Kim, Y.-M. Kim, Y.-T. Kim, J.-H. Nam, Metabolic tumour volume and total lesion glycolysis, measured using preoperative 18f–fdg pet/ct, predict the recurrence of endometrial cancer, BJOG: An International Journal of Obstetrics & Gynaecology 121 (9) (2014) 1097–1106.

[9] M. Machtay, F. Duan, B. A. Siegel, B. S. Snyder, J. J. Gorelick, J. S. Reddin, R. Munden, D. W. Johnson, L. H. Wilf, A. DeNittis, N. Sherwin, K. H. Cho, S.-K. Kim, G. Videtic, D. R. Neumann, R. Komaki, H. Macapinlac, J. D. Bradley, A. Alavi, Prediction of survival by [18F]fluorodeoxyglucose positron emission tomography in patients with locally advanced non-small-cell lung cancer undergoing definitive chemoradiation therapy: results of the ACRIN 6668/RTOG 0235 trial., Journal of Clinical Oncology 31 (30) (2013) 3823–30. doi:10.1200/JCO.2012.47.5947.

[10] S. J. Rosenbaum, T. Lind, G. Antoch, A. Bockisch, False-positive fdg pet uptake- the role of pet/ct, European radiology 16 (5) (2006) 1054–1065.

[11] B. Foster, U. Bagci, A. Mansoor, Z. Xu, D. J. Mollura, A review on segmentation of positron emission tomography images, Computers in biology and medicine 50 (2014) 76–96.

[12] S. Vauclin, I. Gardin, K. Doyeux, S. Hapdey, A. Edet-Sanson, P. Vera, Segmentation des images TEP au $^{18\$}$F-FDG. Principe et revue de la littérature, Médecine Nucléaire 34 (2010) 358–369.

[13] M. Hatt, N. Boussion, C. Cheze-Le Rest, D. Visvikis, O. Pradier, Méthodologies de définition automatique des volumes métaboliquement actifs en tep: évaluation et perspectives, Cancer/Radiothérapie 16 (1) (2012) 70–81.

[14] H. Zaidi, I. E. Naqa, PET-guided delineation of radiation therapy treatment volumes: a survey of image segmentation techniques., European Journal of Nuclear Medicine and Molecular Imaging 37 (11) (2010) 2165–2187. doi:10.1007/s00259-010-1423-3.

[15] W.-Y. Lin, K.-B. Wang, S.-C. Tsai, S.-S. Sun, Unexpected accumulation of f-18 fdg in the urinary

bladder after bladder irrigation and retrograde filling with sterile saline: a possible pitfall in pet examination, Clinical nuclear medicine 34 (9) (2009) 560–563.

[16] R. Boellaard, R. Delgado-Bolton, W. J. Oyen, F. Giammarile, K. Tatsch, W. Eschner, F. J. Verzijlbergen, S. F. Barrington, L. C. Pike, W. A. Weber, et al., Fdg pet/ct: Eanm procedure guidelines for tumour imaging: version 2.0, European journal of nuclear medicine and molecular imaging 42 (2) (2015) 328–354.

[17] F. O. Roberts, D. H. Gunawardana, K. Pathmaraj, A. Wallace, T. Mi, S. U. Berlangieri, G. J. O'Keefe, C. C. Rowe, A. M. Scott, et al., Radiation dose to pet technologists and strategies to lower occupational exposure, Journal of nuclear medicine technology 33 (1) (2005) 44–47.

[18] M. Hatt, C. Cheze le Rest, A. Turzo, C. Roux, D. Visvikis, A fuzzy locally adaptive bayesian segmentation approach for volume determination in pet, Medical Imaging, IEEE Transactions on 28 (6) (2009) 881–893.

[19] M. Hatt, C. Cheze le Rest, P. Descourt, A. Dekker, D. De Ruysscher, M. Oellers, P. Lambin, O. Pradier, D. Visvikis, Accurate automatic delineation of heterogeneous functional volumes in positron emission tomography for oncology applications, International Journal of Radiation Oncology* Biology* Physics 77 (1) (2010) 301–308.

[20] F. Yang, P. W. Grigsby, Delineation of fdg-pet tumors from heterogeneous background using spectral clustering, European Journal of Radiology 81 (11) (2012) 3535–3541.

[21] S. David, D. Visvikis, C. Roux, M. Hatt, Multi-observation PET image analysis for patient follow-up quantitation and therapy assessment., Physics in Medicine and Biology 56 (18) (2011) 5771–5788. doi:10.1088/0031-9155/56/18/001.

[22] L. G. Strauss, P. S. Conti, The applications of pet in clinical oncology., Journal of nuclear medicine: official publication, Society of Nuclear Medicine 32 (4) (1991) 623–48.

[23] R. Xu, D. Wunsch, et al., Survey of clustering algorithms, Neural Networks, IEEE Transactions on 16 (3) (2005) 645–678.

[24] B. J. Frey, D. Dueck, Clustering by passing messages between data points, science 315 (5814) (2007) 972–976.

[25] H.-P. Kriegel, P. Kröger, J. Sander, A. Zimek, Density-based clustering, Wiley Interdisciplinary Reviews: Data Mining and Knowledge Discovery 1 (3) (2011) 231–240.